



Thermodynamic control of tropical cyclogenesis in environments of radiative-convective equilibrium with shear

Eric D. Rappin^{a*}, David S. Nolan^a and Kerry A. Emanuel^b

^a*Rosenstiel School of Marine and Atmospheric Science, University of Miami, Florida, USA*

^b*Program in Atmospheres, Oceans and Climate, Massachusetts Institute of Technology, Cambridge, USA*

*Correspondence to: E. D. Rappin, RSMAS/MPO, 4600 Rickenbacker Causeway, Miami, FL 33149, USA. E-mail: erappin@rsmas.miami.edu

The potential for tropical cyclone formation from a pre-existing disturbance is further explored with high-resolution simulations of cyclogenesis in idealized, tropical environments. These idealized environments are generated from simulations of radiative-convective equilibrium with fixed sea-surface temperatures (SSTs), imposed mean surface winds, and an imposed profile of vertical wind shear. The propensity for tropical cyclogenesis in these environments is measured in two ways: first, in the period of time required for a weak, mid-level circulation to transition to a developing tropical cyclone; and second, from the value of an incubation parameter that incorporates environmental measures of mid-level saturation deficit and thermodynamic disequilibrium between the atmosphere and ocean. Conditions of tropospheric warming can be produced from increased SSTs or from increased mean surface winds; in either case, the time to genesis increases with atmospheric warming. As these parameters are varied, the incubation parameter is found to be highly correlated with changes in the time to genesis.

The high resolution (3 km) of these simulations permits analysis of changes in tropical cyclogenesis under warming conditions at the vortex scale. For increasing SST, increased mid-level saturation deficits (dryness) are the primary reason for slowing or preventing genesis. For environments with increased surface wind, it is the decreased thermodynamic disequilibrium between the atmosphere and ocean that delays or prevents development. An additional effect in both cases is a decoupling of the low-level and mid-level vortices, primarily as a result of increased advecting flow at the altitude of the mid-level vortex, which is linked to the height of the freezing level. Copyright © 2010 Royal Meteorological Society

Key Words: tropical cyclones; surface wind; sea-surface temperature

Received 24 September 2009; Revised 19 August 2010; Accepted 31 August 2010; Published online in Wiley Online Library

Citation: Rappin ED, Nolan DS, Emanuel KA. 2010. Thermodynamic control of tropical cyclogenesis in environments of radiative-convective equilibrium with shear. *Q. J. R. Meteorol. Soc.* **136**: 1954–1971. DOI:10.1002/qj.706

1. Introduction

1.1. Background

Each year, approximately 80 tropical cyclones (TCs) form over the world's oceans. Determination of how TC frequency

and location will fluctuate with climate change is important as a large fraction of the world's population and resources are located in regions susceptible to the high winds, heavy precipitation, storm surge, and inland flooding associated with TCs. The influence of climate change on TC activity is not simple to understand due to the range

of scales involved, from the planetary-scale circulations to the El Niño–Southern Oscillation (ENSO) and the Madden–Julian oscillation, to the mesoscale and even to the cloud scale.

Despite the complexities of the problem, empirical approaches relating TC genesis location and frequency to large-scale conditions have yielded reasonable results. Quantities that are expected to affect the likelihood of tropical cyclogenesis are combined through statistical analysis to produce an empirical genesis potential index (GP). Gray (1979), an early pioneer on the use of a genesis index, favourably connected thermodynamic and dynamic environmental factors to TC climatological frequency.

With the rise in computing power, it has become possible to use global climate models (GCMs) as a tool to understand the influence of the large-scale environment on TC activity. Recent studies (Sugi *et al.*, 2002; Oouchi *et al.*, 2006; Yoshimura *et al.*, 2006; Bengtsson *et al.*, 2007) have utilized GCMs to reproduce TC activity and to predict the level of TC activity in warmer climates. To improve upon the coarse resolution employed by GCMs, regional downscaling, in which a regional model is driven by GCM boundary conditions, has been applied to the problem (Knutson and Manabe, 1998; Knutson and Tuleya, 2004; Knutson *et al.*, 2007, 2008). Another approach is that of Emanuel (2006a) and Emanuel *et al.* (2008, hereafter E08), in which the climate state is randomly seeded with nascent TCs that move according to a beta-and-advection model and whose intensity evolution is determined by a simple but high-resolution coupled TC model. This approach has also been applied to the problem of the effects of climate change on TC activity. To date, such downscaling techniques do not adequately resolve the cloud scale.

1.2. A pseudo-index

For all of its success, Gray's index is tied to current climatological conditions through the use of a fixed sea-surface temperature (SST) value. To expand the applicability of the genesis index to different climates, Emanuel and Nolan (2004) developed a more generalized index to relate past, present, and future climate states to TC activity:

$$GP = |10^5 \eta|^{3/2} \left(\frac{H}{50}\right)^3 \left(\frac{V_{\text{pot}}}{70}\right)^3 (1 + 0.1 V_{\text{shear}})^{-2}, \quad (1)$$

where η is the absolute vorticity, H is the mid-level relative humidity, V_{pot} is the potential intensity as defined by Bister and Emanuel (2002), and V_{shear} is the 850–200 hPa vertical shear. The index is able to reproduce seasonal variations in both hemispheres, and Camargo *et al.* (2007) showed that it is able to capture interannual variations, particularly those associated with ENSO. Despite these successes, the index suffers from several flaws. Most glaring is its dimensional inconsistency. Moreover, recent studies by Nolan *et al.* (2007, hereafter N07) and Nolan and Rappin (2008, hereafter N08) showed that the index predicted an increase in genesis in an environment of increasing SST, whereas numerous GCM simulations with and without regional downscaling show a general decrease in genesis with increasing SST due to global warming (Sugi *et al.*, 2002; Yoshimura *et al.*, 2006; Bengtsson *et al.*, 2007; Emanuel *et al.*, 2008; Knutson *et al.*, 2008), albeit with much regional variability.

As a step towards a new genesis index, one aimed at rectifying the shortcomings noted above, it is worthwhile to establish the climate sensitivities of an established candidate parameter. Recently, E08 discussed the quantity χ_m , an important parameter of Emanuel's Coupled Hurricane Intensity Prediction System (CHIPS) model (Emanuel *et al.*, 2004), the magnitude of which may correlate well with the approximate time-scale for intensification of an incipient tropical cyclone-like disturbance. It is defined as

$$\chi_m = \frac{s_b - s_{\text{mid}}}{s_0^* - s_b}. \quad (2)$$

Here s_{mid} , s_b , and s_0^* are the moist entropies of the mid-troposphere, the boundary layer, and the sea surface at saturation, respectively. The moist entropy is approximately (Emanuel, 1994)

$$s = c_p \ln T - R_d \ln p + \frac{L_v q}{T} - R_v q \ln H, \quad (3)$$

where c_p is the heat capacity of dry air, R_v and R_d are the gas constants for water vapour and dry air, respectively, L_v is the latent heat of vaporization, q is the specific humidity, and H is the relative humidity.

As discussed in E08, χ_m , derived from the assumption of boundary-layer quasi-equilibrium (Raymond, 1995; Emanuel, 1995a), measures the relative importance of subsidence across the boundary-layer top, be it through convective or non-convective motions, as indicated by the numerator (hereafter referred to as χ_{mid}), as compared to the effect of surface fluxes (the denominator, hereafter referred to as χ_{flux}) on the boundary-layer entropy. Larger values of χ_{mid} indicate greater sub-saturation of the mid-levels, leading to a longer incubation period as convective episodes moisten the middle atmosphere and diminish the impact of convective downdraughts. The incubation period here is defined as the time to genesis of an initial precursor disturbance. Likewise, a decrease in χ_{flux} implies reduced surface fluxes (or rather decreased thermodynamic disequilibrium between the ocean surface and the overlying air), diminishing both convective activity and any possible wind-specific humidity feedback such as wind-induced surface heat exchange (WISHE). Note that the numerator of (2) can be written approximately as $s_{\text{mid}}^* - s_{\text{mid}}$, since in convective regions, the boundary-layer entropy, s_b , is nearly equal to the saturation entropy of the free troposphere, s_{mid}^* . This is the condition that a parcel lifted reversibly and adiabatically from the boundary layer have the same temperature as the free troposphere, so that it is approximately convectively neutral. Using the definition of entropy (3) and ignoring the last term of this definition as it is comparatively small.

$$s_{\text{mid}}^* - s_{\text{mid}} \approx L_v \frac{q_{\text{mid}}^* - q_{\text{mid}}}{T_{\text{mid}}}. \quad (4)$$

This shows that the inhibiting effect of middle-troposphere dryness scales as the saturation deficit, not as the relative humidity per se. This suggests that relative humidity used in the earlier definition of GP given by (1) should be replaced by the saturation deficit, or by its non-dimensional equivalent given by χ_m . Of course, as long as the temperature of the middle troposphere is approximately constant in space and time, calibrating (1) on variations in

the current climate cannot reveal the deficiency of using relative humidity in place of saturation deficit. However, under global warming, the variation with temperature of the saturation specific humidity proves to be an important source of the variation in saturation deficit, as demonstrated by E08. Thus we will look at the ability of χ_m to predict the incubation period of seed vortices placed in explicitly simulated radiative-convective equilibrium (RCE) states in the hopes that it may be a suitable parameter for an updated genesis potential index.

A review of the methodology is discussed in section 2. Section 3 provides an overview of the RCE simulations and the thermodynamic parameters of the RCE state. Results of the tropical cyclogenesis simulations will be provided in section 4, with close attention paid to (i) how the results relate to the indices and parameters of section 3 and (ii) the thermodynamic and kinematic evolution of seed vortices placed in various radiative-convective equilibrium states. Finally, a concluding discussion is presented in section 5.

2. Methodology and experimental design

To date, computational resources do not permit the simultaneous resolution of the planetary and convective scales. For this reason, previous work has focused on the response of TC frequency to changing large-scale conditions while failing to adequately resolve the intense cores of TCs. Not surprisingly, as resolution is increased, the simulated structure improves and the number of storms increases (Bengtsson *et al.*, 2007). Likewise, Camargo *et al.* (2007) found that increased resolution provides a more accurate representation of climatology in the genesis index. It is clear that increased resolution better represents the processes vital to tropical cyclogenesis. Therefore, the premise of this study is to approximate the large scale and resolve the convective scale. The objective is to obtain a more thorough understanding of how TCs initialized with a finite-amplitude precursor disturbance respond to changes in idealized, large-scale environmental conditions.

The large-scale environment used in this study is one of RCE as it permits the mapping of the TC response to changing environments in a minimal environmental parameter space. In fact, just two environmental parameters largely control the RCE state, the SST and the mean surface wind (hereafter denoted by u_m). For this reason, the simulations conducted for this study will employ variations in SST and u_m . There is both observational and theoretical evidence that suggest that the likelihood of genesis is related to mean surface wind. An observational study by Emanuel (2006b) noted a significant increase in hurricane activity concurrent with a decrease in mean surface wind over the North Atlantic main development region. Finally, Emanuel (2007) showed that the potential intensity of tropical cyclones is inversely proportional to the mean surface wind speed.

The experimental set-up in this study mimics that of N07 and N08. First, a full physics simulation of random convection is conducted on a 150 km square, doubly periodic grid to achieve a state of RCE. The mean sounding from this RCE state, taken as the horizontal mean of 6-hourly output over the last 30 days of a 90-day simulation, is then used to initialize a simulation of tropical cyclogenesis from a

10 m s⁻¹, mid-level, cold-core vortex on a 1200 km square, doubly periodic grid.

The model used for this study has been updated to the Weather Research and Forecast (WRF) version 2.2.1 mesoscale numerical weather prediction system (Skamarock *et al.*, 2005). All simulations take place on an f -plane with a Coriolis parameter of $5 \times 10^{-5} \text{s}^{-1}$. The horizontal grid spacing has been reduced from 4 km to 3 km for all simulations. The number of vertical levels remains at 40, equally spaced in the WRF hydrostatic pressure vertical coordinate (stretched in height with 10 vertical levels below 2 km). The number of horizontal grid points was kept at 50×50 for the RCE simulations, but increased to 400×400 grid points to maintain a 1200 km square grid for the TC simulations.

Physical parametrizations include the Yonsei University (YSU) boundary layer (Hong *et al.*, 2006) with modifications to the drag formulation following Donelan *et al.* (2004) and implemented by Davis *et al.* (2008) in the WRF model. The WRF single-moment 6-class scheme (Hong and Lim, 2006) is used for microphysical processes. Radiation physics is handled by the Rapid Radiative Transfer Model (RRTM) for long-wave radiation (Mlawer *et al.*, 1997; Iacono *et al.*, 2000) and the Goddard scheme (Chou *et al.*, 1998) for short-wave radiation. Due to the lengthy integration period required for RCE, a perpetual equinox is used while maintaining a diurnal cycle. Convection is explicitly modelled.

All of the simulations, including the initial RCE simulations, include a 5 m s⁻¹, 850–200 hPa piecewise linear shear profile in which the wind profile is constant from the surface up to 850 hPa and from 200 hPa to the domain top. To incorporate vertical shear in a doubly periodic domain without large-scale temperature gradients, the method introduced in N08 was used. A more detailed explanation of their method is provided in the Appendix. A detailed description of the TC initialization can be found in N07. Briefly, the azimuthal wind profile is calculated from the radial integration of a Gaussian vorticity distribution such that a maximum wind, v_{max} , of 10 m s⁻¹ is located at the radius of maximum winds (RMW), taken to be 100 km. The vertical structure uses Gaussian decay above and below the height of the maximum wind, z_{max} . For the simulations here, a value of $z_{\text{max}} = 3.72$ km is used and the vertical decay rate chosen so that the maximum surface wind has exactly one half the value of v_{max} , or 5 m s⁻¹. This structure is modelled after several case-studies of circulations within east Pacific easterly waves (Raymond *et al.*, 1998).

3. Radiative-convective equilibrium simulations

The tropical environment in radiative-convective equilibrium is characterized by a balance between surface moist enthalpy fluxes and column-integrated radiative cooling (Figure 1). N07 contains a detailed discussion on the use of RCE in high-resolution simulations. Although idealized, RCE is a useful thermodynamic state for numerical simulations as it allows a minimum number of parameters to define a single temperature and humidity profile for a given SST. One such parameter is mean surface wind which, as can be seen in Figure 1, has a significant impact on the RCE state. As discussed in N07, the RCE state is characterized by a small number of convective cores, randomly spaced in the domain. As the mean surface wind increases, the quasi-random nature of the convection, the result of symmetric

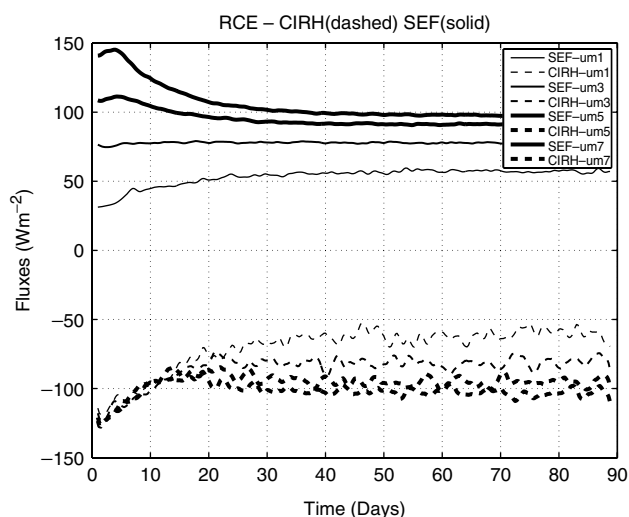


Figure 1. Horizontal mean of column-integrated radiative heating (CIRH, dashed) and surface enthalpy fluxes (SEF, solid). All units are W m^{-2} .

cold pool expansion, is replaced by quasi-organized convection forced by the asymmetric, down-wind expansion of the cold pools (not shown). Not surprisingly, the larger the magnitude of u_m , the larger the surface fluxes, leading to more rapid boundary-layer destabilization and recovery times and hence the more rapid onset of RCE.*

For weak surface winds (1 m s^{-1}), organization of convection is minimal, a result in sharp contrast to the simulations without shear in N07 as shown in Figure 2. Without shear, there is partial aggregation, with organization into moist and dry patches, as described by Bretherton *et al.* (2005) and N07. Aggregation refers to a radiative-convective-moisture feedback where moist convective regions experience enhanced vertical motion and dry patches are susceptible to additional subsidence. This additional secondary circulation is believed to arise as an imbalance of the differential radiational cooling where there is decreased cooling in columns with significant cloud and moisture in comparison to the dry patches. The only partial aggregation seen here may be due to the inability to generate secondary circulations within the small domain, consistent with the findings of Bretherton *et al.* (2005). When shear is included in the simulation, aggregation does not occur for any value of u_m , as the shear is effective in spreading out the convectively generated moisture anomalies, eliminating any radiative-convective feedback and leaving the domain homogenized with respect to water vapour path.

The thermodynamic soundings produced for variable SST at $u_m = 5 \text{ m s}^{-1}$ and variable u_m at $\text{SST}=30.0^\circ\text{C}$ are shown in Figure 3(a, b, c) and 3(d, e, f) respectively. For variable SST, the relative humidity profiles are nearly constant as SST increases, with only small variations occurring above 4 km. Conversely, above the boundary layer there is a large increase in the saturation deficit with its value nearly doubling between $\text{SST}=27.5^\circ\text{C}$ and $\text{SST}=32.5^\circ\text{C}$ in the mid-troposphere around 3 km. For variable u_m , both the relative humidity and the saturation deficit show some variation above the boundary layer, but that variation is small compared to that seen in the boundary layer itself,

*The boundary layer hereafter will refer to the sub-cloud layer.

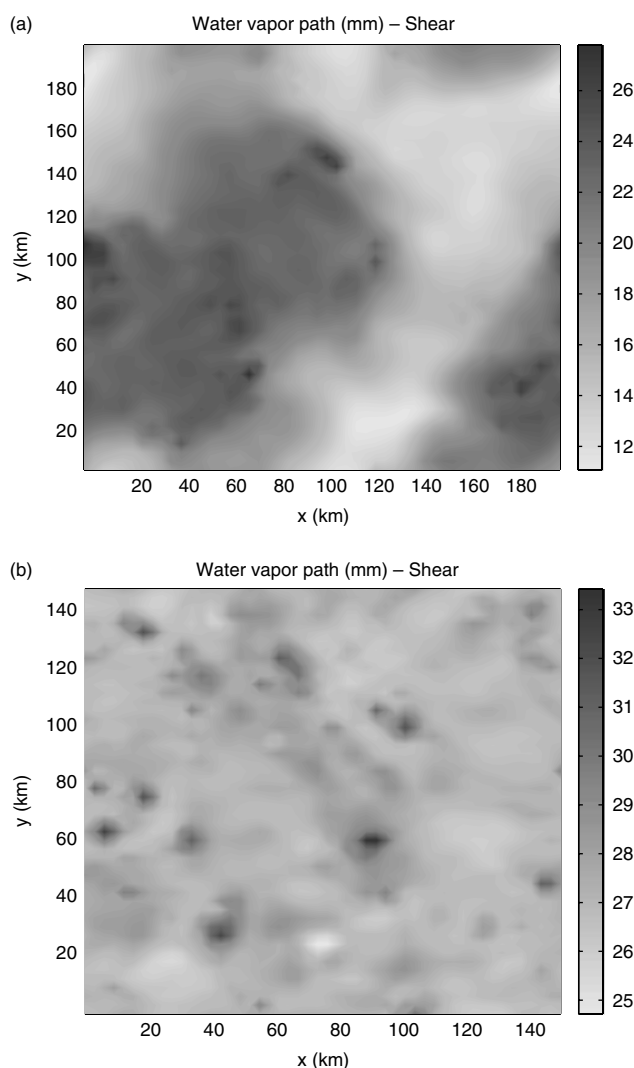


Figure 2. Aggregation in RCE as seen in the column in the vertically integrated water vapour content for $\text{SST}=27.5^\circ\text{C}$ and $u_m = 1$: (a) without shear, 4 km resolution, and (b) with 850–200 hPa shear of 5 m s^{-1} , 3 km resolution.

where the value of saturation deficit is reduced by a third between $u_m = 1 \text{ m s}^{-1}$ and $u_m = 7 \text{ m s}^{-1}$. Note that there is warming throughout the depth of the troposphere for both increasing SST and u_m (Figure 3(c, f)).

Table I gives the values of CAPE, potential intensity, and χ_m , as given by (2), for various values of SST and u_m . The mid-tropospheric entropy s_{mid} , was evaluated at 600 hPa for the calculation of χ_m in (2). For any value of mean surface wind, a 2.5°C increase in SST yields a fractional increase in both potential intensity and χ_m that decreases with increasing SST. At fixed SST, changes in χ_m and V_{pot} are inversely related and nonlinear, with a diminishing fractional change for increasing u_m . These relationships can be seen clearly in Figure 4. RCE states for variable shear were also computed, but the changes in thermodynamic properties discussed here are insignificant for changes in shear compared to the changes induced by varying SST and mean surface wind.

As mentioned in the introduction, larger values of χ_m result from increases to either SST or mean surface wind speed, which are associated with an increasing ‘time to genesis’. Therefore, χ_m will hereafter be referred to as an incubation index. While increasing the SST

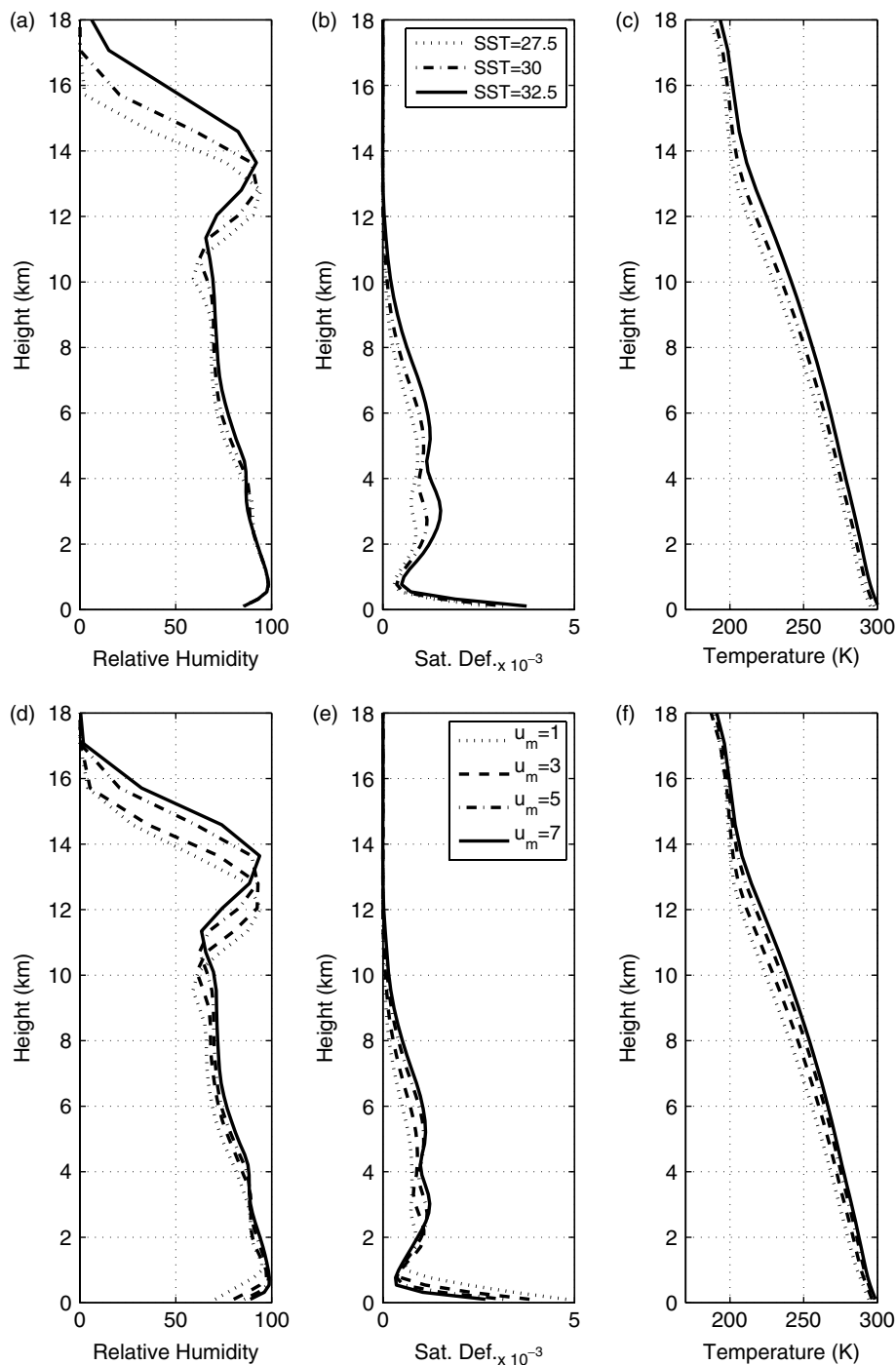


Figure 3. RCE soundings of relative humidity, saturation deficit, and temperature as a function of (a, b, c) SST and (d, e, f) u_m .

does increase the surface thermodynamic disequilibrium (Figure 5), the dependence is relatively weak and is over-matched by the increase in the saturation deficit of the free troposphere (Figures 3(b), 5). In terms of Figure 5, such an effect can be seen as a smaller fractional change in χ_{flux} (dashed lines) compared to the fractional change in χ_{mid} (solid lines) as SST is varied. On the other hand, increasing the mean surface wind speed dramatically reduces the surface thermodynamic disequilibrium and at the same time increases the mid-tropospheric temperature, thereby also increasing the saturation deficit (Figures 3(e), 5); the two effects thus reinforce each other in this case.

One important consideration is that the simulations here reflect warming environments in the absence of additional CO_2 forcing. With larger CO_2 concentrations, enhanced infrared absorption produces upper-level warming above and beyond that which is seen by increasing the SST or u_m in an RCE environment. Additionally, increased surface absorption of infrared radiation would lead to surface temperature increases, which in turn would lead to increased long-wave cooling and increased evaporation, both of which will affect the potential intensity and χ_m . The extent to which CO_2 concentrations affect potential intensity and incubation indices is beyond the scope of this idealized study. Knutson and Tuleya (2004) is just one example of a study that evaluated

Table I. Thermodynamic parameters for atmospheres generated by small-domain simulations of RCE for various values of the environmental parameters SST and u_m .

u_{mid}		SST ($^{\circ}$ C)		
		27.5	30.0	32.5
1.0	CAPE	953	1285	1668
	V_{pot}	67.5	72.5	76.3
	χ_m	0.045	0.054	0.065
3.0	CAPE	1390	1769	2213
	V_{pot}	59.2	63.3	66.9
	χ_m	0.063	0.080	0.097
5.0	CAPE	1621	2051	2507
	V_{pot}	52.5	55.9	59.4
	χ_m	0.078	0.100	0.120
7.0	CAPE	1726	2128	2624
	V_{pot}	47.6	50.8	54.2
	χ_m	0.083	0.107	0.131

Units: u_m and V_{pot} are $m\ s^{-1}$; CAPE is $J\ kg^{-1}$.

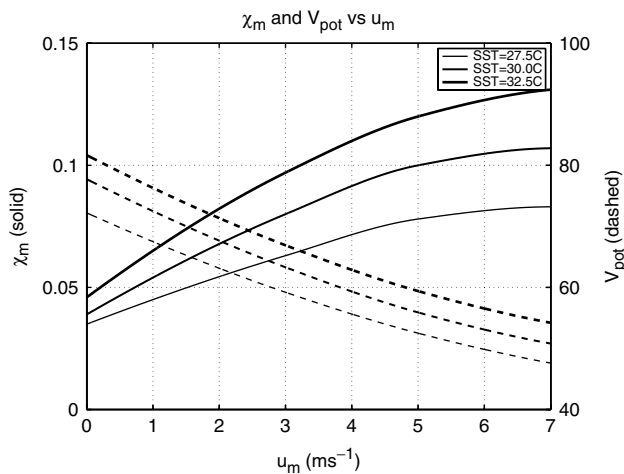


Figure 4. χ_m (solid) and V_{pot} (dashed) as a function of both SST and mean surface wind speed, u_m .

the impacts of increased CO_2 forcing on tropical cyclone intensity.

4. Simulated genesis

The following section will describe the high-resolution simulations of tropical cyclogenesis for our array of RCE environments. Analysis will be applied to a subset of the simulations to provide greater insight into the behaviour of tropical cyclogenesis under shifts in large-scale climatic quantities. The reader is referred to N08 for a description of the evolution of simulations with variable initial vortex strength and for simulations of variable shear for a given SST and u_m .

4.1. Time to genesis and the incubation index

A key aspect of this study is to explore TC development in the range of RCE states given in Table I by use of an incubation index, χ_m (2). To generate a relationship between the TC evolution and χ_m , we assume that some measure of the ‘time

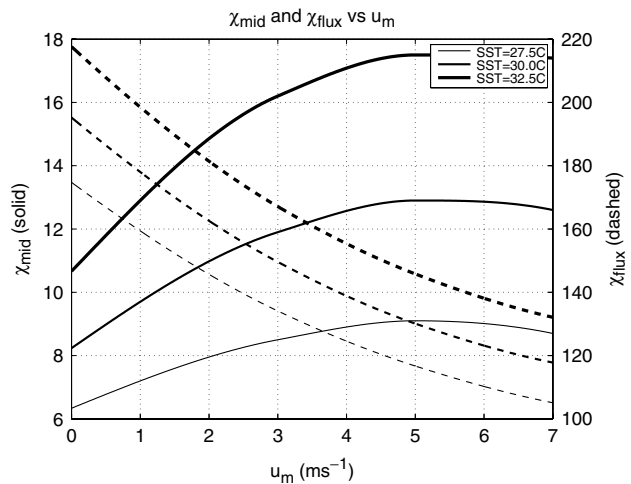


Figure 5. χ_{mid} (solid) and χ_{flux} (dashed) as a function of both SST and mean surface wind speed, u_m .

to genesis’ as seen in the initial vortex simulations can serve as a proxy for the likelihood of genesis for the corresponding RCE state. N07 provides a detailed discussion on the ‘time to genesis’ and how a proxy was determined. Suffice it to say, the definition of genesis is highly subjective outside of the fact that it occurs at or before rapid intensification. In the N07 study, a consistent measure of genesis was found, through trial and error, to be the first time an 8-hour pressure fall reaches a rate equal to 25% of the fastest pressure fall. Presently, a review of the old objective measures and the introduction of a new measure will be made for the new set of simulations presented in this study. Note that increases in value of both χ_m and the proxy correspond to an increase in the incubation period.

The minimum surface pressure traces of Figure 6 show that, for constant u_m , overall intensity increases as SST increases, as expected from potential intensity theory. However, there is little change in the time to rapid intensification except at the extreme values of u_m and SST. For constant SST however, time to rapid intensification increase dramatically with increasing mean surface wind, with no intensification seen at high u_m , even at high SST. It appears that simulated genesis is significantly more sensitive to mean surface wind than to SST.

Table II shows the time to genesis as given by three objective methodologies. The proxies p_{max} and p_{qtmax} represent the time to maximum pressure fall and the time at which the 8-hour pressure fall was 25% the maximum 8-hour pressure fall. The values given in parentheses are proxy values that have been normalized by the control-case value, taken to be the simulation with a SST of $30^{\circ}C$ and $u_m = 5\ m\ s^{-1}$. A new measure, labeled θ_{ediff} , provides an objective algorithm based on structural changes of the vortex. An example of how the measure is calculated is shown in Figure 7. First, the surface vortex is located using a minimum in the smoothed surface pressure field. After taking an azimuthal average of the θ_e field, the radial gradient of the perturbation θ_e (difference between a given value and the value at the same level at 150 km from the centre) is calculated and smoothed ten times with a 1-2-1 filter to eliminate isolated extrema and general noisiness associated with differentiation. A difference in the θ_e values is then taken between 15 km on either side of the minimum in the radial gradient. The calculation is conducted at model

Table II. Objective measures, or proxies, for the time to genesis (hours) for various values of the environmental parameters SST and u_m . Numbers in parentheses represent the values normalized by the control simulation value.

u_m (m s ⁻¹)	Proxy (hours)	SST (°C)		
		27.5	30.0	32.5
1.0	p_{\max}	57 (0.45)	60 (0.47)	60 (0.47)
	p_{qtmax}	18 (0.20)	22 (0.24)	33 (0.37)
	$\theta_{e\text{diff}}$	49 (0.45)	45 (0.42)	45 (0.42)
3.0	p_{\max}	69 (0.54)	72 (0.56)	183 (1.43)
	p_{qtmax}	45 (0.50)	39 (0.43)	65 (0.72)
	$\theta_{e\text{diff}}$	63 (0.58)	59 (0.55)	144 (1.33)
5.0	p_{\max}	135 (1.05)	128 (1.00)	–
	p_{qtmax}	70 (0.78)	90 (1.00)	–
	$\theta_{e\text{diff}}$	81 (0.75)	108 (1.00)	–
7.0	p_{\max}	164 (1.28)	–	–
	p_{qtmax}	111 (1.23)	–	–
	$\theta_{e\text{diff}}$	155 (1.44)	–	–

p_{\max} represents the time to the maximum pressure fall.

p_{qtmax} is the time to an 8-hour pressure fall that is one quarter the maximum fall rate.

$\theta_{e\text{diff}}$ represents the difference between θ_e values straddling the minimum θ_e gradient.

A dash indicates that no genesis time was found.

level 10, which is approximately 2.2 km altitude. To pinpoint a genesis time, several threshold values need to be set; a minimum acceptable θ_e difference and a minimum duration for which the minimum θ_e difference is maintained. Given the large range of values used for the mean surface wind and SST, differing dynamic and thermodynamic evolutions are observed, leading to a wide range of potential threshold values. However, through trial and error, threshold values of 2.25 K for the θ_e difference and 36 hours for the time duration yield consistent values throughout the spectrum of simulations discussed here.

Comparison of the times to genesis of each of the measures with the pressure traces of Figure 6 provides useful insights. For the measure p_{\max} , the times given are clearly too long. This is not surprising as genesis precedes rapid intensification. The second two methods produce genesis times at more realistic pressures. p_{qtmax} genesis times occur in the tropical depression stage (1010–1005 hPa) while $\theta_{e\text{diff}}$ yields genesis times in the tropical storm stage (1002–997 hPa).

It is clear from Tables I and II and Figure 6 that, while χ_m increases with SST due to the nonlinear growth of the saturation deficit with temperature, the time to genesis proxies are relatively constant except at the largest values of SST and u_m . One way to bring χ_m and the proxies closer together in value is to note that V_{pot} portrays a similar increase in value with SST as χ_m . Thus, it is possible to combine these two quantities in an inverse form to mitigate the SST dependence. To maintain the dimensionless nature of χ_m , the ratio $V_{\text{shear}}/V_{\text{pot}}$ is used as the multiplying factor:

$$\gamma = \frac{V_{\text{shear}}}{V_{\text{pot}}} \chi_m, \quad (5)$$

where γ is a modified form of the incubation parameter.

Table III shows the normalized values of χ_m and γ for the RCE states considered. While γ does show an SST dependence, it is significantly smaller than that observed in χ_m . In both parameters a threshold value of 1 appears to distinguish between developing and non-developing cases.

Table III. Incubation parameters for atmospheres generated by small-domain simulations of RCE for various values of the environmental parameters SST and u_m .

u_m (m s ⁻¹)		SST (°C)		
		27.5	30.0	32.5
1.0	χ_m	0.45	0.54	0.65
	γ	0.37	0.42	0.48
3.0	χ_m	0.63	0.80	0.97
	γ	0.60	0.71	0.81
5.0	χ_m	0.78	1.00	1.20
	γ	0.83	1.00	1.13
7.0	χ_m	0.83	1.07	1.31
	γ	0.97	1.18	1.35

Values have been normalized by the value from the control simulation.

χ_m is a non-dimensional parameter that measures the relative importance of convective downdraughts and surface enthalpy fluxes on the subcloud-layer entropy.

γ , or the incubation index, is χ_m multiplied by the ratio of the vertical wind shear to the potential intensity.

γ acts to decrease the SST dependence of the incubation period measure.

Table IV. Correlations between each of the three ‘time to genesis’ proxies and the incubation parameters χ_m and γ .

Proxy	Incubation parameter	
	χ_m	γ
p_{\max}	0.80	0.83
p_{qtmax}	0.77	0.94
$\theta_{e\text{diff}}$	0.76	0.82

Table IV shows the correlation values between the time to genesis, χ_m , and the incubation index. A good correlation is seen in each case, particularly for those between γ and the time to genesis proxies.

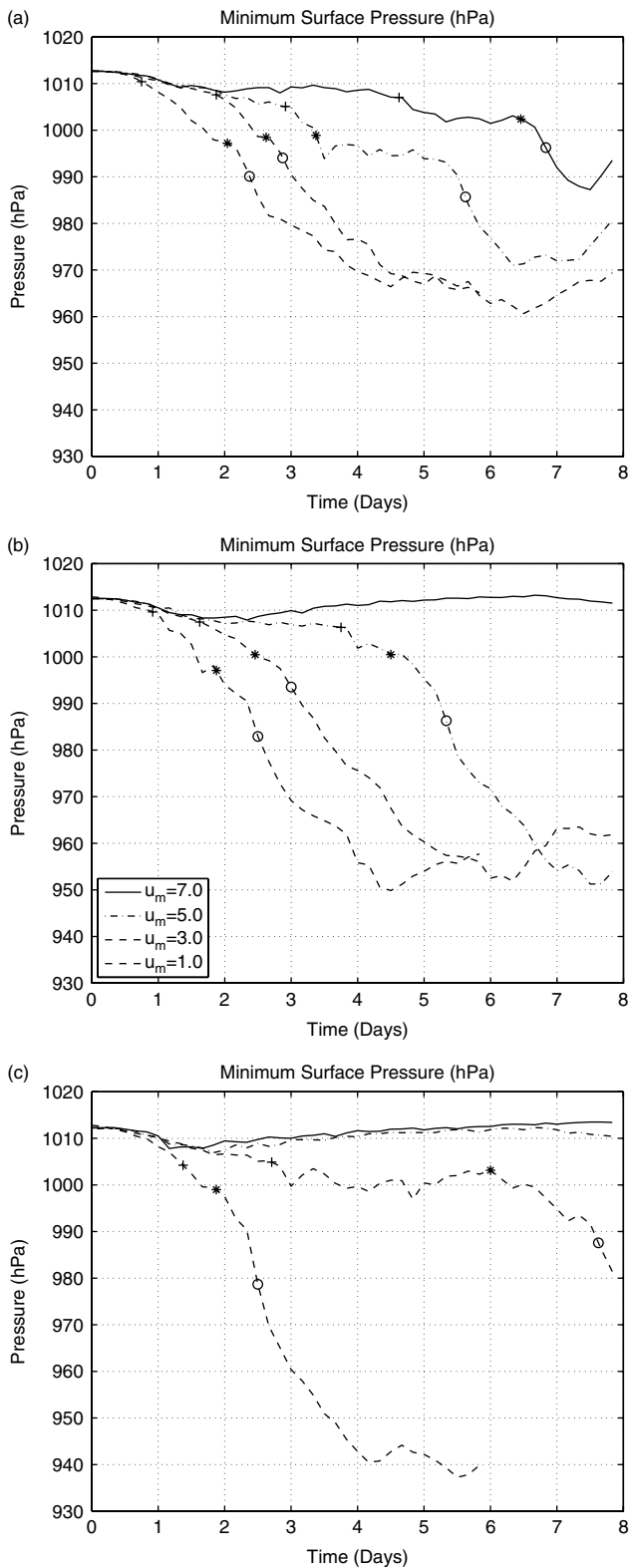


Figure 6. Surface pressure (hPa) traces for the initial vortex simulations with SST = (a) 27.5 °C, (b) 30.0 °C, (c) 32.5 °C. The time to genesis proxies are P_{\max} (\circ), $P_{qt\max}$ (+), $\theta_{e\text{diff}}$ (*).

4.2. Theory

As proposed by Kleinschmidt (1951) and Riehl (1954), latent and sensible heat fluxes from the sea surface are crucial to TC genesis and intensification. Decades of numerical simulations have verified the fundamental role of surface fluxes (Ooyama, 1969; Rotunno and Emanuel,

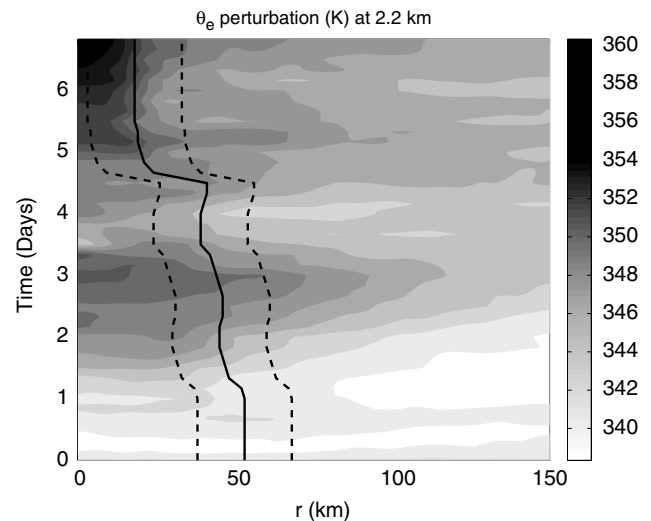


Figure 7. θ_e perturbation with $\min(d\theta_e/dr)$ given by the solid black contour. The two dashed contours show the locations at which the time to genesis proxy $\theta_{e\text{diff}}$ is calculated. See text for additional details.

1987; Nguyen *et al.*, 2008). While several theories have been developed to explain tropical cyclogenesis, all rely on air–sea fluxes. The vortical hot tower (VHT) route of intensification (Hendricks *et al.*, 2004) requires the heat and moisture from surface fluxes to maintain the buoyant VHTs (Nguyen *et al.*, 2008). Likewise, the WISHE feedback relies on the positive feedback between the increasing cyclonic winds of a deepening TC and the boundary-layer entropy gradients via increases in boundary-layer entropy by surface fluxes.

One impact of warming the troposphere, either through increased surface fluxes or increased SST in RCE, is the shift of the sounding toward a warmer moist adiabat. As the troposphere warms, the dry static stability increases due to the increasing influence of water vapour on latent heating. Such a change in static stability may have a significant impact on the mass flux and the resiliency of the vortex to shear (Jones, 1995; Smith *et al.*, 2000; Reasor *et al.*, 2004). It should be noted that the most significant divergence among moist adiabats occurs in the upper troposphere (Figure 3(c, f)), so a change in the coupling of the low- and mid-level vortex by change in stability may not be significant.

4.3. Simulation results

Due to the relatively high resolution used in this study relative to GCMs, it is possible to examine exactly how the simulated systems evolve at the cloud-resolving scale (i.e. the physical processes related to tropical cyclogenesis) and to relate contrasting cases with their environments. For the sake of brevity, only three of the cases presented in Figure 6 will be discussed: one developing and two non-developing cases. The developing case is characterized by SST=30 °C and $u_m = 5 \text{ m s}^{-1}$ (CONTROL). The non-developing cases are for a higher mean surface wind, SST=30 °C and $u_m = 7 \text{ m s}^{-1}$ (WIND) and a higher SST, SST=32.5 °C and $u_m = 5 \text{ m s}^{-1}$ (WARM). Based on the previous discussion of the incubation index χ_m , we learned that a large saturation deficit is characteristic of the warmer SST RCE states while decreased thermodynamic disequilibrium is indicative of the large mean surface wind

RCE states. It is our goal to verify the impact of these characteristics on our high-resolution simulations through a kinematic and thermodynamic investigation.

4.3.1. Kinematic perspective

A companion piece to this study will provide an in-depth quantitative analysis of genesis for various shear profiles where changes in kinematic as opposed to thermodynamic evolution are easier to elucidate. For this study, the variations in thermodynamic states do influence the kinematic evolution, so a qualitative description of the evolution will be discussed.

For simulation CONTROL, the kinematic evolution is displayed in plots of the column-integrated water vapour or the water vapour path (WVP), surface winds, and mid-level geopotential height shown in Figure 8. Note that the domain in the figure is just over one quarter of the total simulation domain and centred on the surface vortex. Mid-level geopotential height, smoothed for clarity, characterizes mid-level (550 hPa) development. At hour 36, the strongest convection can be found on the down-shear flank of the surface vortex, corresponding to the imposed vertical shear (westerly at 5 m s^{-1}) and enhanced boundary-layer convergence associated with translational motion. The mid-level vortex has been advected well down-shear, with quasi-balanced forced subsidence in its wake. At the centre of the mid-level height minimum, a mesoscale divergence pattern can be observed in the surface wind field ($x = 150 \text{ km}$, $y = 100 \text{ km}$). Twenty-four hours later (Figure 8(b)), the mid-level vortex has continued down-shear to $x = 250 \text{ km}$ and $y = 100 \text{ km}$. A long zonal line of convection has developed where the strong southerlies of the primary flow impinge upon the mesoscale outflow, similar to that observed in the numerical simulations of Davis and Galarneau (2009). The region of mesoscale divergence at the surface has expanded as the mid-level vortex has decayed, with the maximum in convergence being maintained in the down-shear-left quadrant of the surface vortex. Such a configuration is characteristic of a mesoscale convective system (MCS). While the MCS and the zonal convective line have mostly decayed by day 3 (Figure 8(c)), a new convectively generated mid-level vortex has formed where the maximum convergence was found 12 hours previously. Finally, at day 4 (Figure 8(d)), the convection has organized and the mid-level vortex has intensified and begun to migrate inward toward the centre of the surface circulation. There was a brief period of intensification during this convective organization between days 3 and 4. For the next 12 hours, the mid-level vortex oscillates between the down-shear and down-shear left flank of the surface vortex as the vortex tilt decreases (not shown) until the circulation becomes vertically stacked and rapid intensification commences.

Experiment WARM displays much more active convection early in the simulation (Figure 9(a)) compared to CONTROL (Figure 8(a)). Much like the other simulations, a zonal line of convergence develops between the primary circulation and the mesoscale divergence pattern ($x > 0 \text{ km}$, $y = 0 \text{ km}$). Despite the strong convection, the mid-level vortex has become completely decoupled from the low-level vortex 24 hours later and the surface mesoscale divergence pattern has propagated toward the edge of the figure ($y = 150 \text{ km}$) as shown (Figure 9(b)). A large downdraught (indicated by anomalously low WVP) at $x = 0 \text{ km}$,

$y = 100 \text{ km}$ has penetrated the low-level core, halting any deepening of the surface disturbance. Advancing 36 hours (Figure 9(c)), the boundary layer has recovered and there is active convection over a significant area of the surface vortex. A second, weak region of low-level divergence has developed beneath the mid-level low, a region fed by significant convection to its south. Again, a downdraught in the core can be seen at $x = 50 \text{ km}$, $y = 100 \text{ km}$. This downdraught is devastating as the already weakened surface circulation is disrupted by the noticeably strong outflow. Finally at day 5, there is little organization to the convection other than the widespread convective/stratiform activity being limited to the down-shear side of the surface trough by subsidence on the up-shear side.

The early evolution of simulation WIND mimics that of the previous two simulations. By 60 hours (Figure 10(b)), convection has developed along the zonal convergence region. While the strongest convection is still found on the down-shear flank of the surface vortex, a significantly weaker geopotential height anomaly, compared with CONTROL, is realized (Figure 10(c)). Additional convection has developed in the region of weak convergence along the surface trough axis. Convection has become widespread and loosely organized by day 4 (Fig 10(d)). The mid-level circulation has filled and there is no longer a trace of easterly flow on the north side of the vortex.

To address more closely the vortex evolution during these simulations, Figure 11 shows time–height plots of relative vorticity averaged over a box, 300 km on each side, centred on both the surface vortex and the vortex at 5 km height, for each of the three cases. In each case following the mid-level vortex, the simulation initiates with the development and lifting of the mid-level vortex, in which periods of deep convection and stratiform processes feed the mid-level vorticity, through heating above and cooling below the freezing level. Such a diabatic heating profile leads to the formation of a mesoscale convective vortex (MCV) near the melting level roughly 36 hours into each simulation. At, or just prior to 2 days, a rapid collapse in low-level vorticity is seen in all cases due to downdraught-driven low-level divergence beneath the mid-level vortex (Bister and Emanuel, 1997, their Figure 13(a)).

From the perspective of the surface vortex, mid-level vorticity rapidly diminishes as the developing MCV advects down-shear. There is intensification at low levels, around 2 km and below, following the surface vortex. Such an increase is attributed to sustained convection on the down-shear flank of the surface vortex. At 2 days, the evolutions of the developing and non-developing cases deviate. For CONTROL, there is a shift in the location of the mid-level vortex after 60 hours. At this time, the mid-level low associated with the sustained convection on the down-shear-left flank of the surface vortex becomes deeper than that of the down-shear MCV. Thus there is a rapid decrease in mid-level vorticity followed quickly by the development of a vertical column of low- and mid-level vorticity at $t = 2.67$ days associated with a discrete jump in position found by the tracking algorithm.

The two non-developing cases continue to track the downstream MCV. Prior to day 4, WARM begins to show rejuvenation as discussed previously. This re-intensification is short-lived as convective downdraughts ultimately cool the boundary layer and disrupt the low-level circulation.

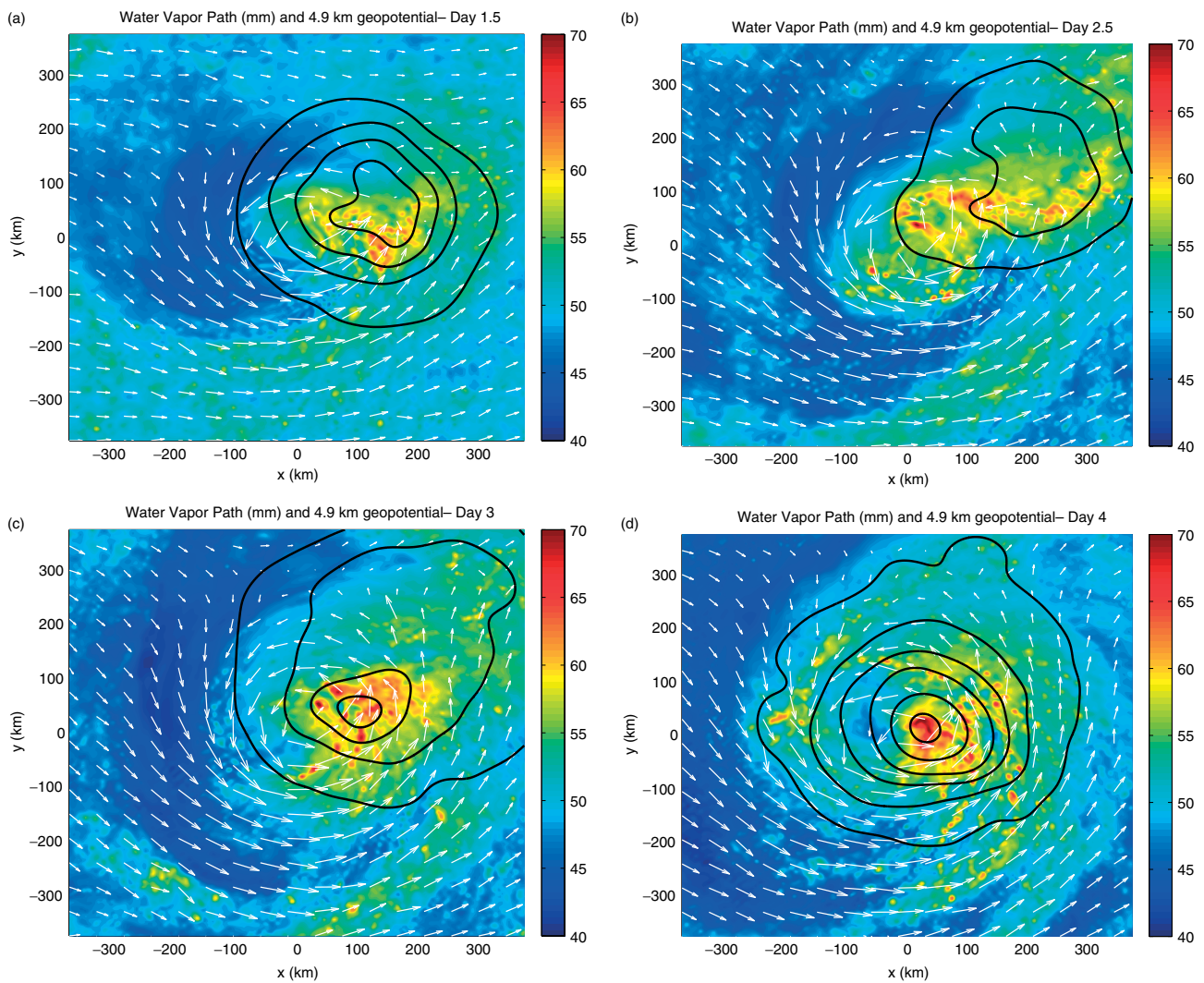


Figure 8. Experiment CONTROL: water vapour path (mm, shading), surface wind (vectors), and ϕ at 550 hPa (contours decreasing inwards: 4.875, 4.870, 4.865, 4.860, 4.850, 4.835 km) for (a) 1.5 days, (b) 2.5 days, (c) 3 days, and (d) 4 days. The 700 km \times 700 km region shown is less than that of the entire model domain, and is centred on the surface vortex.

Finally, a significant feature of Figure 11 is the higher-altitude development of the mid-level MCV in experiment WARM, and to a lesser extent in WIND, compared with experiment CONTROL. This observation, as shown by the increasing altitude of the freezing level (dashed contours of Figure 11), is a consequence of the warmer troposphere of simulations WIND and WARM and plays a role in the coupling (or lack thereof) between surface and developing mid-level vortices.

The results presented here appear to be robust in an ensemble sense. N07, using the same methodology applied in this study to three cases with different random perturbations to the initial low-level temperature field, showed that there was no variation in either the genesis or the rapid intensification stages, suggesting the various stages of evolution are controlled by the initial vortex and the RCE state. N08 provided results similar to that of experiment WARM, with the formation of destructive convective downdraughts that inhibit intensification, using a coarser resolution and a different random distribution of low-level temperature perturbations. Finally, the pressure traces of Figure 6 show a systematic variation with the variations of either SST or mean surface wind.

To summarize the development for simulation CONTROL, it is the sustained convergence between the primary circulation and the low-level outflow boundary beneath the MCV on the down-shear-left flank of the surface vortex, a region of little saturation deficit, that results in persistent, organized, deep convection that warms the troposphere and leads to mid-level height falls and eventually a vertically stacked vortex. Such an evolution is reminiscent of the down-shear development previously identified by Molinari *et al.* (2004).

4.3.2. Thermodynamic perspective

We now return to the incubation parameter χ_m to explore the thermodynamic nature of the simulations. The two terms that compose the incubation parameter are intimately related to moist (saturated) static energy and its budget. Specifically, the surface fluxes and the time rate of change of the column-integrated saturation deficit (CISD) are two terms in the column-integrated saturation static energy budget.

Figure 12 displays the CISD (Figure 12(a)), here normalized by the mass per unit area, or $\int \rho dz$, and the surface enthalpy fluxes as a function of zonal direction

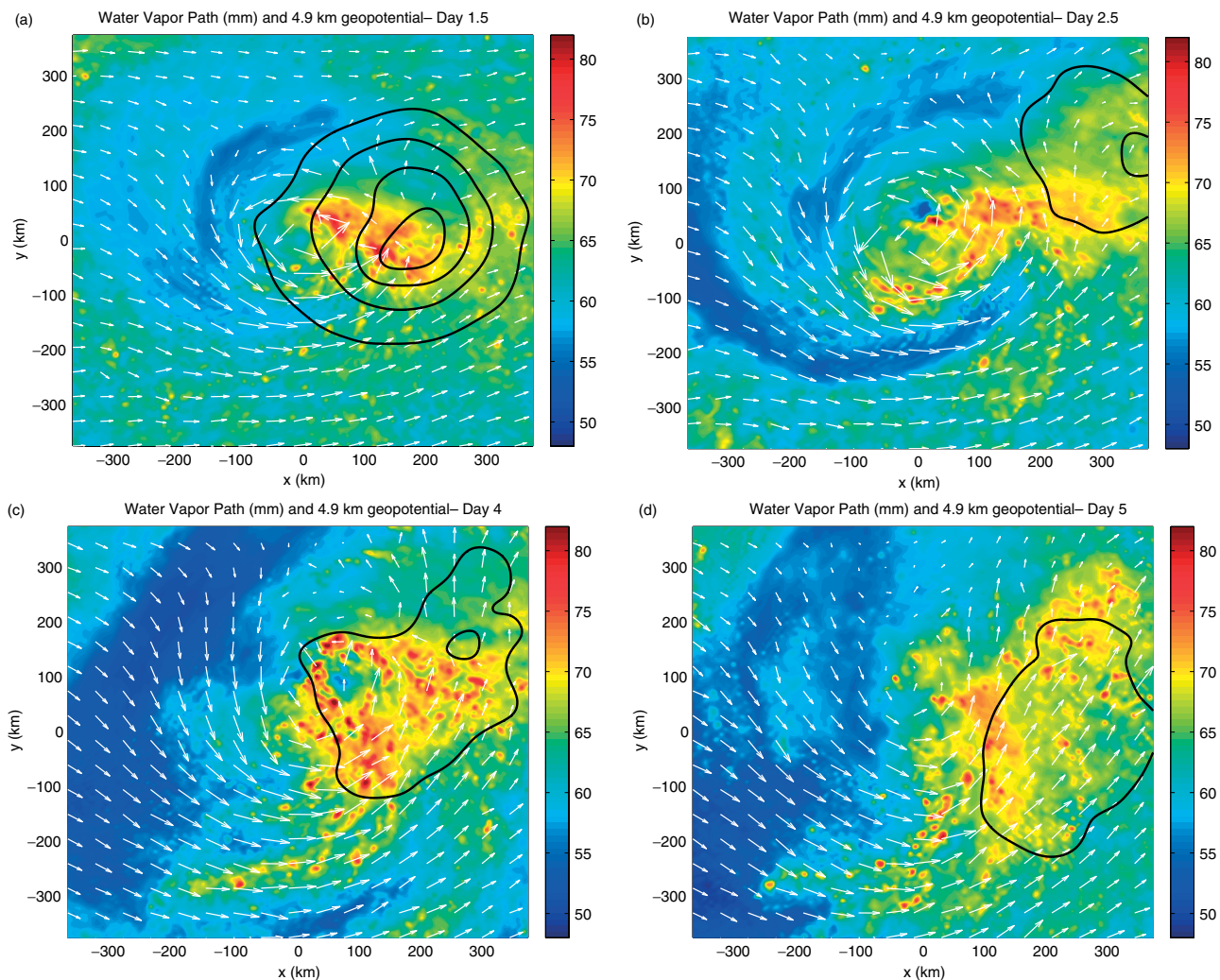


Figure 9. As Figure 8, but for Experiment WARM, and with 550 hPa ϕ contours at 4.916, 4.911, 4.906, 4.901 km for (a) 2 days, (b) 3 days, (c) 5 days, and (d) 6 days.

and time (Figure 12(b)). Each quantity has been averaged meridionally between 75 km north and south of the surface pressure minimum. Note how CISD reflects the shear-generated vertical motion asymmetry with low values down-shear, reflecting near saturation conditions, and large values up-shear, reflecting the subsidence drying occurring there. The time evolution of CISD also reflects the kinematic evolution discussed in the previous section with regard to simulation CONTROL. Prior to day 2, the down-shear translation of the mid-level vortex is observed. After 60 hours, near $x = 100$ km, development of a new mid-level vortex is seen (Figure 8(c)). As observed in the advancement of low values of CISD towards the surface vortex centre, from 72 to 96 hours the vortex tilt decreases in magnitude. The time between days 4 and 5, the pre-intensification stage, is the genesis stage according to the $\theta_{e,diff}$ genesis proxy. Finally, from day 5 on rapid intensification is occurring.

Figure 12(b) displays the surface enthalpy fluxes along the zonal direction through the storm core which have been meridionally averaged like the CISD. It is evident that two branches of enhanced surface fluxes exist early in the evolution of simulation CONTROL. On the down-shear flank, enhanced fluxes are the result of convective gustiness and hence are maximized prior to day 2 when the mid-level vortex has decoupled from the surface circulation. Enhanced fluxes on the up-shear flank are the result of enhanced

thermodynamic disequilibrium. On the northern flank of the vortex, the cyclonic circulation is offset by the westerly mean surface wind. The absence of a net surface wind results in weak fluxes and dry boundary-layer air which is advected cyclonically into the western flank of the surface vortex. Note that the magnitude of this anomaly is greater than the one produced by convective gustiness and, not surprisingly, occurs later in the evolution. Furthermore, both flanks of enhanced fluxes expand outward with time, leaving a minimum over the surface circulation centre. The up-shear fluxes continuously expand outward with time as subsidence drying is coupled with the outward cyclonic movement of low-level dry air from the northern flank. This time evolution of dry air can be observed in the Figure 8 time series. The down-shear flank is limited in its expanse as the new mid-level vortex development constrains the outward growth.

At the end of day 3, the beginning of the pre-intensification stage, we can see a more symmetric distribution of fluxes though a strong, narrow, down-shear asymmetry does develop (Figure 12(b)). Recall that just prior to this time, the vortex tilt diminished as near column-integrated saturation set in over the down-shear hemisphere of the surface circulation. The near-saturated conditions means that the energy input into the column from the surface fluxes go largely into heating the column rather than moistening it (outside of the moistening needed to maintain the

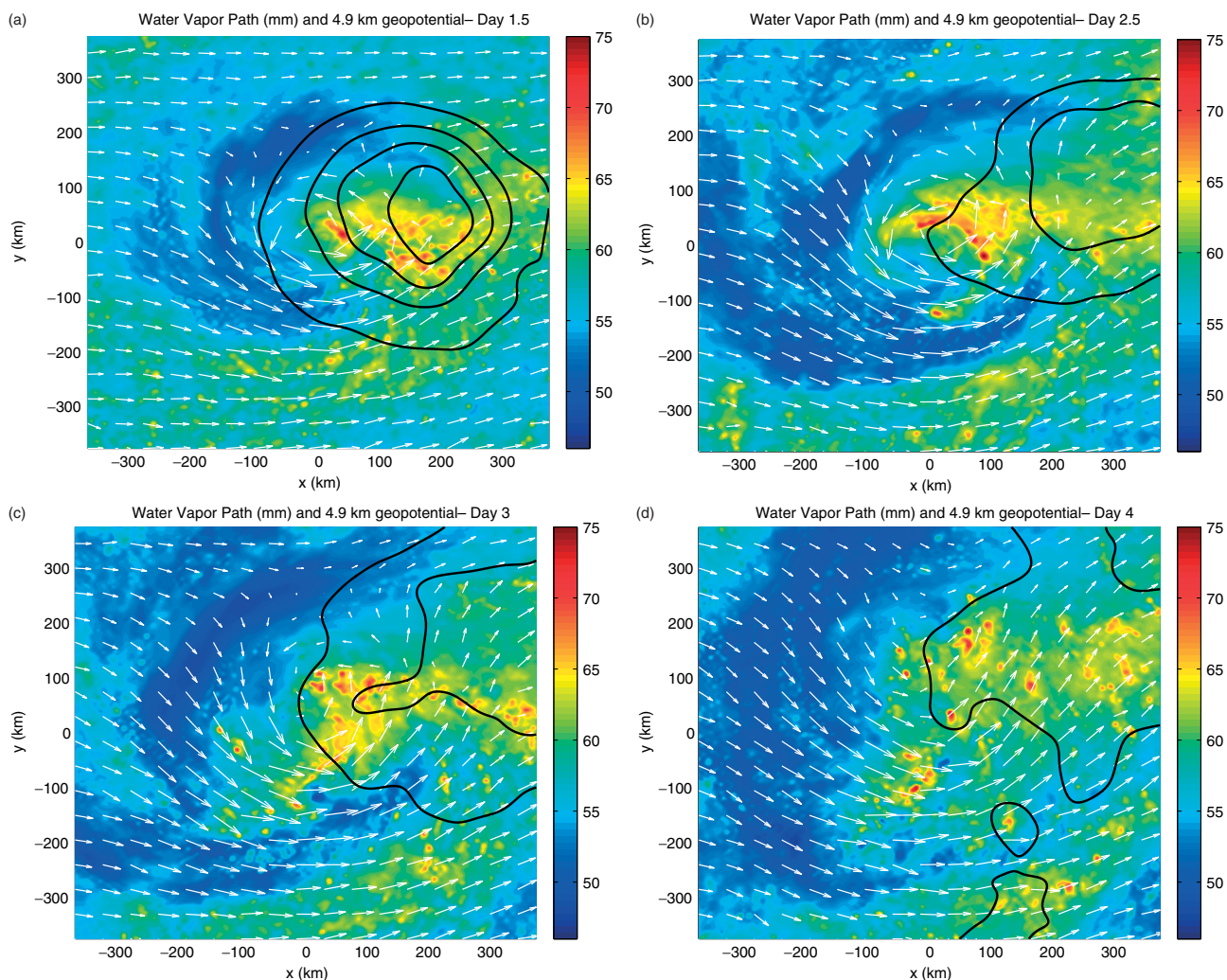


Figure 10. As Figure 8, but for Experiment WIND, and with 550 hPa ϕ contours at 4.898, 4.893, 4.888, 4.883 km for (a) 1.5 days, (b) 2.5 days, (c) 3 days, and (d) 4 days.

near-saturated conditions as the column warms). Such column warming can be seen in Figure 13, which portrays the column-integrated dry static energy (CIDSE), again normalized by the mass per unit area. Since CIDSE is controlled by the column-integrated temperature, there is an up-shear bias in large-valued CIDSE due to the adiabatic warming and drying on the up-shear flank, as seen in the CIRD shown in Figure 12(a). Note that between 60 and 90 hours on the down-shear flank, after development of a new mid-level circulation and prior to the rapid-intensification phase, the CIDSE is nearly constant in time as diabatic heating is offset by adiabatic cooling. During the pre-intensification stage, we begin to see an increase in CIDSE in a region of low CIDSE.

Once near-saturation sets in, column heating produces a 6 to 7 hPa pressure fall by day 4.5 (Figure 6(b)). From a quasi-equilibrium viewpoint, the boundary-layer moist static energy (MSE) of the near-saturated core can increase by surface fluxes unimpeded due to the small vertical MSE gradient across the boundary-layer top. Convection in the incipient vortex can communicate the increased MSE into the free troposphere, leading to warm core development and the WISHE feedback. Since the distribution of vertical motion becomes more skewed towards updraughts in a nearly saturated environment (Nolan, 2007), strong downdraught-driven surface divergence is largely absent

and surface vorticity convergence spins up the surface circulation. Hence at day 4.5, the genesis time given by the $\theta_{e\text{diff}}$ genesis proxy, we see the development of strong symmetric surface fluxes (Figure 12(b)) and rapid intensification commences just 6 hours later (Figure 6(b)).

Recall from the kinematic discussion that convective downdraughts appeared to be the disruptive force in simulation WARM. Examination of the magnitude and distribution of CIRD for simulation WARM (Figure 14(a)) confirms this hypothesis. While the CIRD plot shows the familiar down-shear propagation of the original mid-level vortex, by day 2 there is a 20% fractional increase in CIRD over the surface core. Such large saturation deficits prohibit saturation on the mesoscale and therefore warming of the boundary layer. Thus, strong downdraughts dominate the evolution of Figure 9 despite the presence of significant thermodynamic disequilibrium. The surface enthalpy fluxes (Figure 14(b)) largely mimic those of simulation CONTROL through 2.5 days. With the inability to generate a new mid-level vortex, the surface fluxes slowly decrease in magnitude on the down-shear flank as the parent vortex fills. Nevertheless, enhanced fluxes are maintained well into the integration due to convective gustiness (Figure 9(b, c)). Also note the larger magnitude down-shear fluxes relative to simulation CONTROL. Here the convective gustiness is

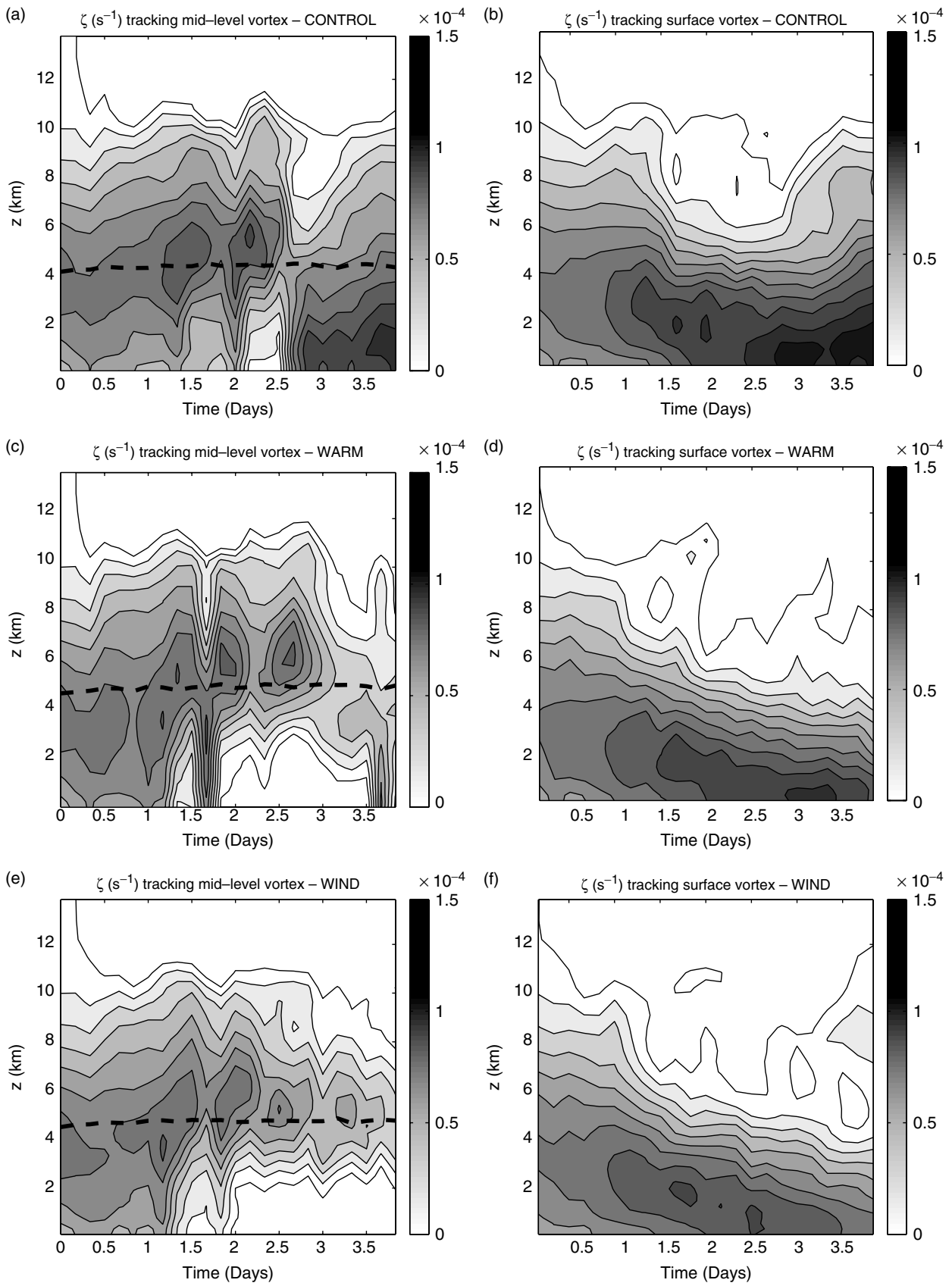


Figure 11. Time–height diagrams of relative vorticity (s^{-1}) in a box of length 300 km. The box is centred over the smoothed minimum in geopotential at 550 hPa for experiments (a) CONTROL, (c) WARM, and (e) WIND. The 273.15 K contour is shown as dashed. (b, d, f) are as (a, c, e), but the box is centred over the smoothed minimum in surface pressure.

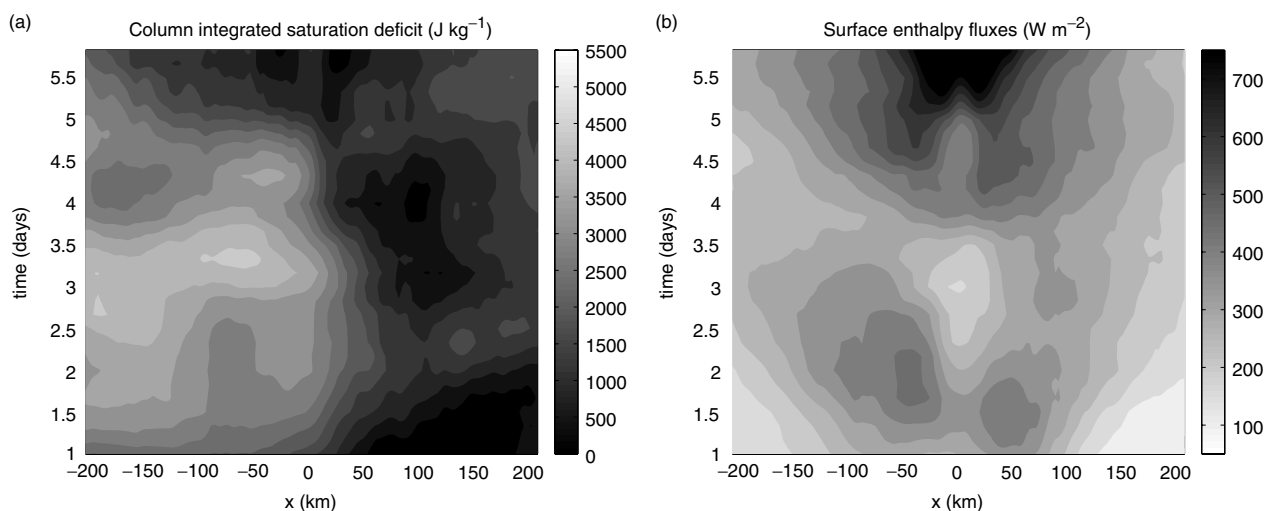


Figure 12. Experiment CONTROL: Zonal section of meridionally averaged (a) column-integrated saturation deficit (J kg^{-1}) normalized by mass per unit area and (b) surface enthalpy fluxes (W m^{-2}). The meridional average is 150 km in length centred on the surface vortex.

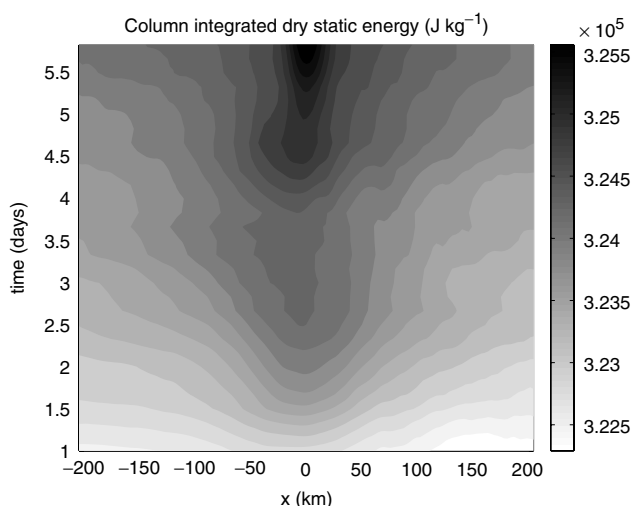


Figure 13. Experiment CONTROL: Zonal section of meridionally averaged column-integrated dry static energy (J kg^{-1}) normalized by mass per unit area. The meridional average is 150 km in length centred on the surface vortex.

stronger due to the higher CAPE environment of simulation WARM (Table I).

Comparing the CISC of simulation WIND (Figure 15(a)) with that of simulation CONTROL (Figure 12(a)) shows they are very close in magnitude and structure. There is a relatively larger CISC over the surface core in simulation WIND, though it is much smaller in magnitude than that of simulation WARM. As the forced convection on the down-shear-left flank is unable to generate a new mid-level vortex, the CISC values do not decrease to the values seen in simulation CONTROL until well after day 4 when the surface wind field has become an open wave (Figure 10(d)).

The surface enthalpy fluxes of simulation WIND (Figure 15(b)) are highly constrained and never approach the magnitude seen in either simulation CONTROL or simulation WARM. From the aerodynamic flux formulation of surface enthalpy fluxes, there must either be a lack of thermodynamic disequilibrium or the absence of a net surface wind. Both mechanisms are at work in simulation WIND. Recall that the environmental sounding

is taken as the mean of the last 30 days of a 90-day convection simulation. With a mean wind of 7 m s^{-1} operating for 90 days, the boundary layer is very close to thermal equilibrium with the ocean surface, as seen in Figure 3(d, e, f). In fact, the thermodynamic disequilibrium at the beginning of simulation WIND is the same as underneath the fully developed TC of simulation CONTROL as well as the $u_m = 1$ and 3 m s^{-1} TC simulations at $\text{SST} = 30^\circ \text{C}$ (not shown). Ekman pumping maintains convection over the surface vortex while the MCS divergent outflow maintains a zonal line of convection where it converges with the primary circulation. Yet the large mean surface winds diminish the impact of convective gustiness. The perturbation surface wind, defined as the difference between the total surface wind and the mean surface wind, u_m , have minimal impact on generating a low-level radial entropy gradient. Therefore, it is the failure of simulation WIND to develop that suggests the fundamental importance of WISHE to genesis (or at least to genesis as defined within this study) and intensification.

Two further simulations were conducted to verify the importance of WISHE on intensification. The cases with $u_m = 3$ and 5 m s^{-1} (CONTROL) at $\text{SST} = 30^\circ \text{C}$ were repeated, but with the surface wind speed capped at 10 m s^{-1} in the calculation of surface moisture and heat fluxes as in Montgomery *et al.* (2009), hereafter M09. The surface fluxes peak at 150 and 220 W m^{-2} for $u_m = 5$ and 3 m s^{-1} respectively, an order of magnitude smaller than the uncapped simulations. The increased surface fluxes for $u_m = 3 \text{ m s}^{-1}$ result from the increased thermodynamic disequilibrium. The results are shown in Figure 16. While both original simulations show development, neither of the capped enthalpy flux simulations produce genesis. These results are in stark contrast to those found in M09 where there is minimal change in the gestation period and comparatively small change in the tangential wind maximum between capped and uncapped simulations. The different results are likely due to the significant differences in the modelling frameworks used in this study and theirs. M09 used 5 km horizontal resolution, no mean flow or wind shear, and simpler physical

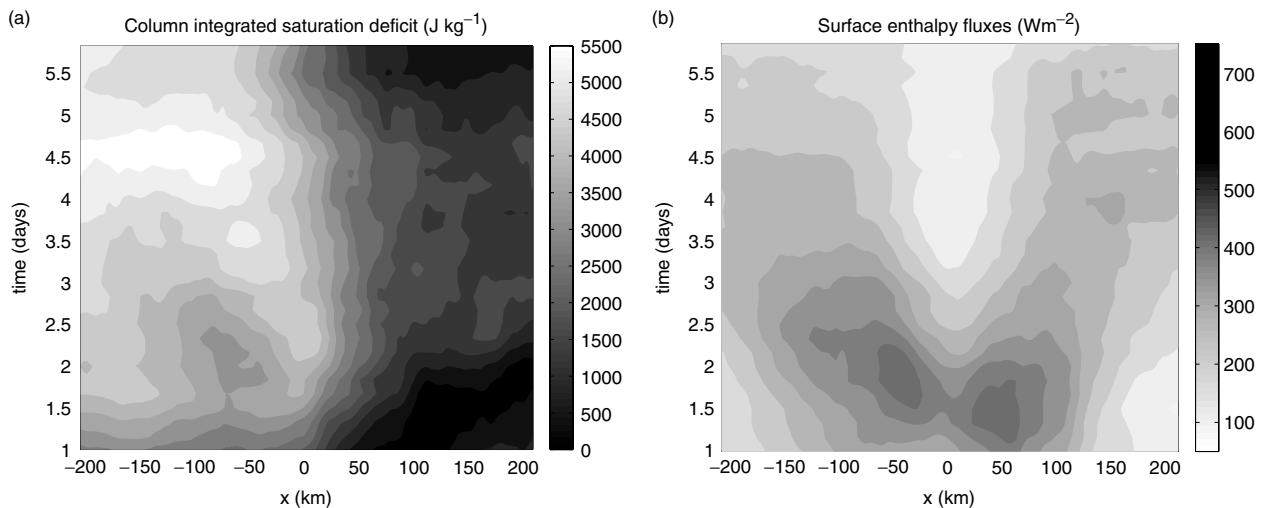


Figure 14. As Figure 12, but for Experiment WARM.

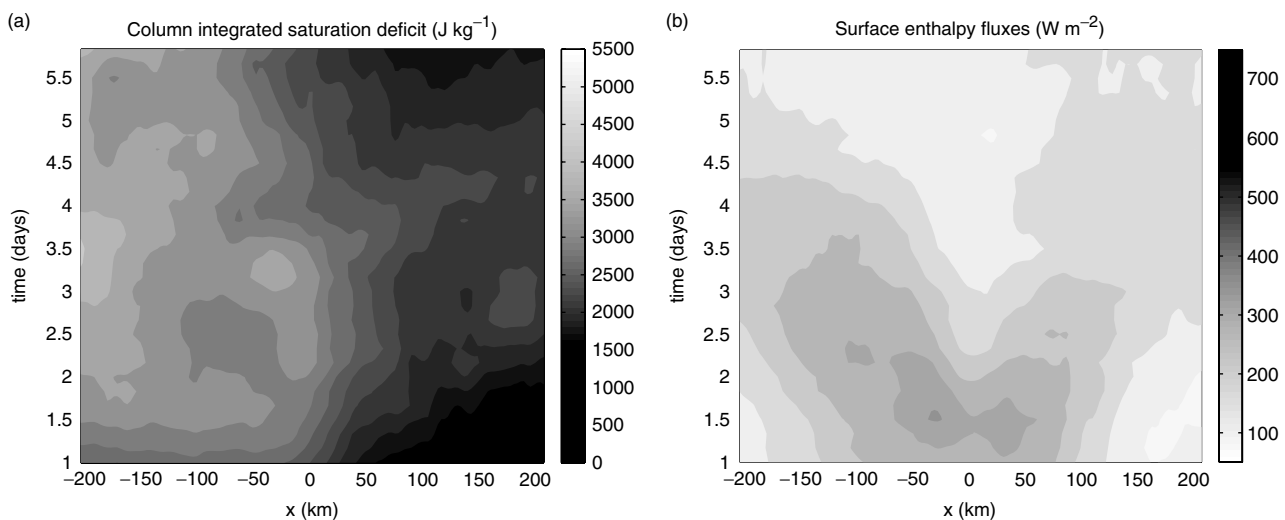


Figure 15. As Figure 12, but for Experiment WIND.

parametrizations, most notably warm rain microphysics without ice processes.

4.3.3. Discussion

Everything else being equal, the rate of intensification should follow the correlation between surface enthalpy fluxes and perturbation column-integrated MSE. Since the atmosphere is in RCE, it is the perturbation surface winds and the degree of thermodynamic disequilibrium that drive the surface fluxes. In addition to surface fluxes, the degree of mid-level saturation controls the MSE, as convection in an unsaturated environment yields convective downdraughts that transport lower values of MSE into the boundary layer to offset the warming by surface fluxes. In the two non-developing cases presented here, either a larger saturation deficit or a lack of thermodynamic disequilibrium is found to explain the thermodynamic factors behind the failure to intensify.

Considering thermodynamic disequilibrium alone, one would anticipate a more rapid intensification of an initial vortex at larger values of SST (Figure 4). When CISD, and the associated dry convective downdraughts, are accounted for, the reverse result is found, that the time to genesis increases for increasing SST. Dynamical effects aid in the

increasing incubation period for increasing SST. As the surface wind asymmetry is fixed, the major change between variable SST simulations is the thermal structure of the troposphere resulting from increased SST or u_m . With tropospheric warming, the altitude of the freezing level increases, the diabatic heating profile shifts upward, and as a result the developing mid-level MCV develops higher up in the shear profile (Figure 13). Essentially, the MCV develops in a stronger advecting flow. Notice how, for $u_m = 5 \text{ m s}^{-1}$, the mid-level circulation becomes decoupled from the surface circulation for $\text{SST} = 32.5^\circ\text{C}$ but does not for $\text{SST} = 30^\circ\text{C}$ (compare Figures 10(b) and 12(b)). A consequence of the decoupling is the vulnerability of the surface core to dry air from the quasi-balanced forced subsidence trailing the MCV. As a result, convection rooted to the surface vortex entrains dry air, producing strong downdraughts (Figure 12(b,c)) that disrupt the circulation and fill the surface depression.

For decreased thermodynamic disequilibrium, the ambient sub-cloud layer environment is so close to saturation that the perturbation surface winds cannot extract additional enthalpy from the sea surface. Convection cannot produce a feedback as there is minimal difference between the saturation specific humidity given by the SST and surface pressure

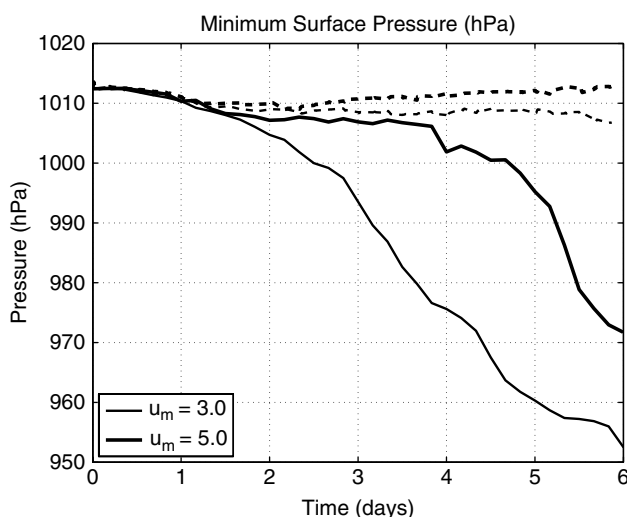


Figure 16. Minimum surface pressure (hPa) traces for the initial vortex simulations with (dashed) and without (solid) capped surface enthalpy fluxes. Simulations had a SST of 30°C and $u_m = 5 \text{ m s}^{-1}$ (bold) and 3 m s^{-1} (thin).

and the actual surface specific humidity (note the decrease in χ_{flux} with u_m as shown in Figure 5). A mean surface wind of 5 m s^{-1} appears to be the threshold for the cases presented here. Above 5 m s^{-1} , decreases in the potential intensity and increases in χ_m lead to very large incubation periods and hence failure to develop within a reasonable time frame. Of course, if the strength of the initial disturbance were increased, the above threshold should increase.

5. Conclusions

Considerable attention has been given to the effects of climate change on tropical cyclogenesis over the past few years. To date, that attention has been given to the large scales in order to grasp the change in planetary-scale circulations, and then to relate these changes to the development of under-resolved tropical cyclones. In this study, we have taken the alternative approach of approximating the large scales through the use of RCE for various values of SST and mean surface wind. These large-scale conditions were then applied to cloud-resolving simulations of tropical cyclogenesis in order to gain a deeper understanding of how a finite-amplitude disturbance evolves in different large-scale environments.

As a step towards a revised genesis index, a dimensionless incubation parameter χ_m , which measures the relative importance of convective downdraughts and surface fluxes, has been compared to the incubation periods of high-resolution simulations of a finite-amplitude precursor disturbance. The incubation parameter does not trend downward with increasing warming, as recent GCM modelling results suggest, but when combined with the potential intensity in a certain functional form, the modified incubation parameter γ can reduce and possibly eliminate the SST dependence. Furthermore, γ does a remarkable job of predicting incubation time for seed vortices in a cloud-resolving model, especially compared with the Emanuel and Nolan genesis potential index.

The major factors that separate development from non-development of finite-amplitude precursor disturbances in the high-resolution numerical simulations presented here

are thermodynamic in nature. As the SST is increased for a given mean surface wind in an environment of RCE, the low- to mid-tropospheric saturation deficit increases significantly. Additionally, warming of the troposphere from an increased SST results in an increased decoupling of low- and mid-level vortices due to an increased altitude of the freezing level and MCV development. Combining the mid-level subsidence drying on the up-shear side of the translating mid-level vortex with the increased low- and mid-level saturation deficit results in strong downdraughts that weaken the surface circulation when convection is triggered over the surface vortex. As the mean surface wind is increased for a given SST, the increase in incubation period is significant compared to the incubation period for changes in SST. This is the result of the humidification of the boundary layer in an RCE environment. As the boundary layer humidifies through increases in surface wind, the thermodynamic disequilibrium asymptotically approaches zero and the magnitude of the anomalous surface enthalpy fluxes are constrained, negating any surface wind–surface flux feedback.

It is important to note that only one specific shear profile was used for this study, one which happened to be parallel to and of the same sign as the mean surface wind. A follow-up study will detail how changes in the direction of the shear relative to the translational motion will effect development in environments of RCE.

Acknowledgements

This work has been supported by the National Science Foundation under grants ATM-0630721 and ATM-0851021. Some of the simulations were performed on the supercomputers at the Computational and Information Systems Laboratory of the National Center for Atmospheric Research and the Center for Computational Science at the University of Miami. The authors are grateful to two anonymous reviewers who provided helpful comments.

Appendix

Since small-domain simulations of RCE necessitate doubly periodic boundary conditions, the inclusion of vertical shear is made difficult by the inability to prescribe a mean horizontal temperature gradient. To maintain the periodicity of the domain with the inclusion of vertical shear, the simulation is initialized with a mean zonal wind profile as a function of pressure, $U(p)$. To balance the corresponding Coriolis force, an additional term is added to the pressure gradient on the right-hand side of the meridional momentum equation:

$$\frac{Dv}{Dt} + fu = -\frac{\partial \Phi}{\partial y} + fU(p). \quad (\text{A.1})$$

The additional term provides the pressure gradient force that would exist if the temperature gradient were present. By maintaining the artificial pressure force throughout the simulation, the desired mean wind shear is maintained throughout the domain. However, the local effects of convection and TC development can locally modify the mean flow, just as would occur in the atmosphere. Furthermore, a realistic, nonlinear Ekman layer develops in the boundary layer, with cross-gradient flow that is unimpeded by domain boundaries.

Of course it is important to acknowledge what is being neglected by this method: (i) the mean temperature gradient, and (ii) adiabatic ascent and descent on sloped potential temperature surfaces, which might result in significant vertical motions and temperature changes for parcels following circular trajectories on sloped potential temperature surfaces in a mid-level vortex. For a mean 850 to 200 hPa shear of 5 m s^{-1} at $f = 5 \times 10^{-5} \text{ s}^{-1}$, the horizontal temperature gradient amounts to $0.6 \text{ }^\circ\text{C}$ per 1000 km; for the same shear, the adiabatic ascent and descent of parcels at the 500 hPa level in a 200 km diameter vortex would result in a change in pressure altitude of about 1.3 hPa and a change in temperature of $0.2 \text{ }^\circ\text{C}$. Thus, the kinematic effects of such a shear profile should dominate over temperature advection and adiabatic ascent.

An important benefit of this approach is that generalization to more complex shear environments with both $U(p)$ and $V(p)$ is straightforward. Another consideration is the neglect of the homogenization of the large-scale potential vorticity gradient associated with the baroclinic environment, which is absent in this experimental design. With a moderate to strong vortex, homogenization of large-scale potential vorticity can allow the vortex to intensify. However, with the weak primary circulation used in this genesis experiment along with a weak large-scale potential vorticity gradient, this mechanism can be considered negligible.

For the simulations presented, a simple shear profile which gives a piecewise linear increase in U in log-pressure height, increasing from a specified surface wind u_m , is used:

$$U(p) = (u_m + C_1) + (C_2 U_{\text{shear}}) \{5 - \log_{10}(p)\}. \quad (\text{A.2})$$

The constants in (A.2) have been chosen so that U_{shear} is the zonal wind speed difference between the 850 and 200 hPa pressure levels, and u_m is the mean surface wind. For a mean surface pressure of 1015 hPa, $C_1 = 0.05 \text{ m s}^{-1}$ and $C_2 = 1.592$. However, if this formula is used for $U(p)$ in the forcing term in (A.1), the nonlinear mixing in the boundary layer changes the wind profile so that it deviates from (A.2). In practice, a first RCE simulation is performed with the nominal constants C_1 and C_2 , and then the deviations of the final equilibrium wind profile from (A.2) are used to estimate corrections to C_1 and C_2 , so that when the new coefficients are applied, the final mean RCE wind profile is very close to that desired.

References

- Bengtsson L, Hodges KI, Esch M, Keenlyside N, Kornbluh L, Luo JJ, Yamagata T. 2007. How may tropical cyclones change in a warmer climate? *Tellus A* **59**: 539–561.
- Bister M, Emanuel KA. 1997. The genesis of hurricane *Guillermo*: TEXMEX analyses and a modeling study. *Mon. Weather Rev.* **125**: 2662–2682.
- Bister M, Emanuel KA. 2002. Low-frequency variability of tropical cyclone potential intensity. I: Interannual to interdecadal variability. *J. Geophys. Res.* **107**: DOI: 10.1029/2001JD000776.
- Bretherton CS, Blossey PN, Khairoutdinov M. 2005. An energy balance analysis of deep convective self-aggregation above uniform SST. *J. Atmos. Sci.* **62**: 4273–4292.
- Camargo SJ, Sobel AH, Barnston AG, Emanuel KA. 2007. Tropical cyclone genesis potential index in climate models. *Tellus A* **59**: 4428–4443.
- Chou M-D, Suarez MJ, Ho C-H, Yan MM-H, Lee K-T. 1998. Parameterizations for cloud overlapping and shortwave single-scattering properties for use in general circulation and cloud ensemble models. *J. Climate* **11**: 202–214.
- Davis CA, Bosart LF. 2006. The formation of hurricane *Humberto* (2001): The importance of extratropical precursors. *Q. J. R. Meteorol. Soc.* **132**: 2055–2085.
- Davis CA, Wang W, Chen SS, Chen Y, Corbosiero K, DeMaria M, Dudhia J, Holland G, Klemp J, Michalakes J, Reeves H, Rotunno R, Snyder C, Xiao Q. 2008. Prediction of landfalling hurricanes with the Advanced Hurricane WRF model. *Mon. Weather Rev.* **136**: 1990–2005.
- Davis CA, Galarneau T Jr. 2009. The vertical structure of mesoscale convective vortices. *J. Atmos. Sci.* **66**: 686–704.
- Donelan MA, Haus BK, Reul N, Plant WJ, Stiassne M, Graber HC, Brown OB, Saltzman ES. 2004. On the limiting aerodynamic roughness of the ocean in very strong winds. *Geophys. Res. Lett.* **31**: L18306, DOI: 10.1029/2004GL019460.
- Emanuel KA. 1994. *Atmospheric Convection*. Oxford University Press: New York.
- Emanuel KA. 1995. The behavior of a simple hurricane model using a convective scheme based on subcloud-layer entropy equilibrium. *J. Atmos. Sci.* **52**: 3959–3968.
- Emanuel KA. 2006a. Climate and tropical cyclone activity: A new model downscaling approach. *J. Climate* **19**: 4797–4802.
- Emanuel KA. 2006b. 'Environmental influences on tropical cyclone variability and trends'. In *Preprints for 27th Conference on Hurricanes and Tropical Meteorology*, Monterey, California. Amer. Meteorol. Soc: Boston.
- Emanuel KA. 2007. Environmental factors affecting tropical cyclone power dissipation. *J. Climate* **20**: 5497–5509.
- Emanuel KA, Nolan DS. 2004. 'Tropical cyclones and the global climate system'. In *Preprints for 26th Conference on Hurricanes and Tropical Meteorology*, Miami, Florida. Amer. Meteorol. Soc: Boston.
- Emanuel KA, DesAutels C, Holloway C, Korty R. 2004. Environmental control of tropical cyclone intensity. *J. Atmos. Sci.* **61**: 843–858.
- Emanuel KA, Sundararajan R, Williams J. 2008. Hurricanes and global warming: Results from downscaling IPCC AR4 simulations. *Bull. Amer. Meteorol. Soc.* **89**: 347–367.
- Gray WM. 1979. Hurricanes: Their formation, structure and likely role in the tropical circulations. In *Meteorology over the Tropical Oceans*, Shaw DB. (ed.) R. Meteorol. Soc: Reading, UK. 155–218.
- Hendricks EA, Montgomery MT, Davis CA. 2004. The role of 'vortical' hot towers in the formation of tropical cyclone *Diana*. *J. Atmos. Sci.* **61**: 1209–1232.
- Hong S-Y, Lim J-O. 2006. The WRF single-moment 6-class microphysics scheme (WSM6). *J. Korean Meteorol. Soc.* **42**: 129–151.
- Hong S-Y, Noh Y, Dudhia J. 2006. A new vertical diffusion package with an explicit treatment of entrainment processes. *Mon. Weather Rev.* **134**: 2318–2341.
- Iacono MJ, Mlawer EL, Clough SA, Moncette JJ. 2000. Impact of an improved radiation model, RRTM, on the energy budget and thermodynamic properties of the NCAR community climate model. *J. Geophys. Res.* **105**(D11): 14873–14890.
- Jones SC. 1995. The evolution of vortices in vertical shear. I: Initially barotropic vortices. *Q. J. R. Meteorol. Soc.* **121**: 821–851.
- Kleinschmidt E. 1951. Grundlagen einer theorie des tropischen zyklonen. *Arch. Meteorol. Geophys. Bioklimatol. Ser. A* **4**: 53–72.
- Knutson TR, Manabe S. 1998. Model assessment of decadal variability and trends in the tropical Pacific Ocean. *J. Climate* **11**: 2273–2296.
- Knutson TR, Tuleya RE. 2004. Impact of CO₂-induced warming on simulated hurricane intensity and precipitation: Sensitivity to the choice of climate model and convective parameterization. *J. Climate* **14**: 2458–2468.
- Knutson TR, Sirutis JJ, Garner ST, Held IM, Tuleya RE. 2007. Simulation of the recent multidecadal increase of Atlantic hurricane activity using an 18 km-grid regional model. *Bull. Amer. Meteorol. Soc.* **88**: 1549–1565.
- Knutson TR, Sirutis JJ, Garner ST, Vecchi GA, Held IM. 2008. Simulated reduction in Atlantic hurricane frequency under twenty-first-century warming conditions. *Nature* **436**: 359–364.
- Mlawer EJ, Taubman SJ, Brown PD, Iacono MJ, Clough SA. 1997. Radiative transfer for inhomogeneous atmosphere: RRTM, a validated correlated-k model for the longwave. *J. Geophys. Res.* **102**(D14): 16663–16682.
- Molinari J, Vollaro D, Corbosiero KL. 2004. Tropical cyclone formation in a sheared environment: A case study. *Mon. Weather Rev.* **61**: 2493–2509.
- Montgomery MT, Nguyen SV, Persing J, Smith RK. 2009. Do tropical cyclones intensify by WISHE? *Q. J. R. Meteorol. Soc.* **135**: 1697–1714.
- Nguyen SV, Smith RK, Montgomery MT. 2008. Tropical-cyclone intensification and predictability in three dimensions. *Q. J. R. Meteorol. Soc.* **134**: 563–582.
- Nolan DS. 2007. What is the trigger for tropical cyclogenesis? *Austral. Meteorol. Mag.* **56**: 241–266.

- Nolan DS, Rappin ED, Emanuel KA. 2007. Tropical cyclogenesis sensitivity to environmental parameters in radiative-convective equilibrium. *Q. J. R. Meteorol. Soc.* **133**: 2085–2107.
- Nolan DS, Rappin ED. 2008. Increased sensitivity of tropical cyclogenesis to wind shear in higher SST environments. *Geophys. Res. Lett.* **35**: L14805, DOI: 10.1029/2008GL034147.
- Oouchi K, Yoshimura H, Mizuta R, Kusunoki S, Noda A. 2006. Tropical cyclone climatology in a global-warming climate as simulated in a 20-km mesh global atmospheric model: Frequency and wind intensity analysis. *J. Meteorol. Soc. Japan* **84**: 259–276.
- Ooyama KV. 1969. Numerical simulation of the life cycle of tropical cyclones. *J. Atmos. Sci.* **26**: 3–40.
- Raymond DJ. 1995. Regulation of moist convection over the west Pacific warm pool. *J. Atmos. Sci.* **52**: 3945–3959.
- Raymond DJ, Lopez-Carillo C, Cavazos LL. 1998. Case studies of developing east Pacific easterly waves. *Q. J. R. Meteorol. Soc.* **124**: 2005–2034.
- Reasor PD, Montgomery MT, Grasso LD. 2004. A new look at the problem of tropical cyclones in vertical shear flow: Vortex resiliency. *J. Atmos. Sci.* **61**: 3–22.
- Riehl H. 1954. *Tropical Meteorology*. McGraw-Hill: New York.
- Ritchie EA, Holland GJ. 1997. Scale interactions during the formation of typhoon *Irving*. *Mon. Weather Rev.* **125**: 1377–1396.
- Rotunno R, Emanuel KA. 1987. An air–sea interaction theory for tropical cyclones. Part II: Evolutionary study using a nonhydrostatic axisymmetric numerical model. *J. Atmos. Sci.* **44**: 542–561.
- Skamarock WC, Klemp JB, Dudhia J, Gill DO, Barker DM, Wang W, Powers JG. 2005. 'A description of the Advanced Research WRF version 2'. Tech. Note 468+STR, NCAR: Boulder, USA.
- Smith RK, Wolfgang U, Sneddon G. 2000. On the dynamics of hurricane-like vortices in vertical-shear flows. *Q. J. R. Meteorol. Soc.* **126**: 2653–2670.
- Sugi M, Noda A, Sato N. 2002. Tropical cyclone climatology in a global-warming climate as simulated in a 20 km mesh global atmospheric model: Frequency and wind intensity analysis. *J. Meteorol. Soc. Japan* **80**: 249–272.
- Yoshimura J, Masato S, Noda A. 2006. Influence of greenhouse warming on tropical cyclone frequency. *J. Meteorol. Soc. Japan* **84**: 405–428.